Tomography of the Solar Corona with the Metis Coronagraph I: Predictive Simulations with Visible Light Images

Alberto M. Vásquez (✉ albert@iafe.uba.ar)
  National Council for Scientific and Technological Research (CONICET) - University of Buenos Aires (UBA)

Federico A. Nuevo
  National Council for Scientific and Technological Research (CONICET) - University of Buenos Aires (UBA)

Federica Frassati
  Istituto Nazionale di Astrofisica (INAF), Osservatorio Astrofisico di Torino, Pino Torinese (To)

Alessandro Bemporad
  Istituto Nazionale di Astrofisica (INAF), Osservatorio Astrofisico di Torino, Pino Torinese (To)

Richard A. Frazin
  University of Michigan

Marco Romoli
  Università degli Studi di Firenze (UniFI)

Nishtha Sachdeva
  University of Michigan

Ward B. Manchester IV
  University of Michigan

Tomography of the Solar Corona with the Metis Coronagraph I: Predictive Simulations with Visible Light Images

Alberto M. Vásquez[1,2] ·

Federico A. Nuevo[1,3] ·

Federica Frassati[4] ·

Alessandro Bemporad[4] ·

Richard A. Frazin[5] · Marco Romoli[6] ·

Nishtha Sachdeva[5] · Ward B. Manchester

IV[5]

Abstract The Metis coronagraph of the Solar Orbiter (SolO) mission records full-Sun images of the solar corona in Lyman-α ultraviolet (UV) radiation and in visible light polarized brightness (pB). This work investigates the utility of a synoptic observational program of Metis in terms of using its pB-images for tomographic reconstruction of the three-dimensional (3D) distribution of the electron density of the global solar corona. During its lifetime, SolO's distance to the Sun will range $D \approx 0.3 - 1.0$ au, while its solar latitude will span $\theta \approx \pm 33°$. The limitations that such orbit complexity poses on tomographic reconstructions is explored in this work. Using SolO's predictive orbital information and 3D MHD simulations of the solar corona, time series of synthetic Metis pB-images were computed and used as data to attempt tomographic reconstruction of

✉ A.M. Vásquez
  albert@iafe.uba.ar

  F.A. Nuevo
  federico@iafe.uba.ar

  F. Frassati
  federica.frassati@inaf.it

  A. Bemporad
  alessandro.bemporad@inaf.it

  R.A. Frazin
  rfrazin@umich.edu

  M. Romoli
  marco.romoli@unifi.it

  N. Sachdeva
  nishthas@umich.edu

  W.B. Manchester IV
  chipm@umich.edu

1   Instituto de Astronomía y Física del Espacio (IAFE), National Council for Scientific and Technological Research (CONICET) - University of Buenos Aires (UBA), Ciudad de Buenos Aires, Argentina

1   Universidad Nacional de Tres de Febrero (UNTREF), Departamento de Ciencia y Tecnología, Caseros, Prov. de Buenos Aires, Argentina

3   Universidad de Buenos Aires (UBA), Ciclo Básico Común (CBC), Ciudad de Buenos Aires, Argentina

4   Istituto Nazionale di Astrofisica (INAF), Osservatorio Astrofisico di Torino, Pino Torinese (To), Italy

5   Department of Climate and Space Sciences and Engineering (CLaSP), University of Michigan, Ann Arbor, MI, USA

6   Dipartimento di Fisica e Astronomia, Università degli Studi di Firenze (UniFI), Firenze, Italy

the model. These numerical experiments were implemented for two Carrington rotations, corresponding to a solar minimum and a solar maximum, representative of extreme conditions of coronal complexity. For each rotation images were synthesized from three orbital segments, corresponding to extreme geometrical conditions of observation by Metis. For the early phase of the mission (year 2023), simulations were carried from the largest aphelion ($D \approx 0.95$ au) and the smallest perihelion ($D \approx 0.29$ au), both cases corresponding to low latitude ($|\theta| < 10°$) positions. For the late phase of the mission (year 2029), a simulation was carried out from the maximum solar latitude position ($\theta \approx +33°$), at an intermediate distance ($D \approx 0.5$ au). The range of heights that can be reconstructed and the required data-gathering time, both dependent on D, are reported for the six experiments. The extension of the coronal region that can be reconstructed and the accuracy of the reconstruction, both decreasing with increasing solar latitude $|\theta|$ as well as with increasing coronal complexity, are discussed in detail in each case. As a general conclusion, a Metis synoptic observational program with a cadence of at least 4 images/day provides enough data to attempt tomographic reconstructions of the coronal electron density during the whole lifetime of the mission, a requirement well within the $2 - 3$ hr cadence of the current synoptic program. This program will allow implementation of tomography experimenting with different values for the cadence of the time-series of images used to feed reconstructions. Its cadence will also provide continuous opportunity to select images avoiding highly dynamic events, which compromise the accuracy of tomographic reconstructions.

Keywords: Observations; Spectrum, Visible; Corona, Structures; Corona, Models; Solar Cycle

1. Introduction

One of the most direct diagnostics of the electron density of the solar corona is provided by its free electrons Thomson scattering the intense photospheric visible light (VL) radiation (Minnaert, 1930). Methods to determine the three-dimensional (3D) structure of the electron density of the corona based on VL images date back to the pioneering work by van de Hulst (1950), which used eclipse images assuming azimuthal symmetry. Since then, methods have evolved into modern solar rotational tomography (SRT) techniques, which make no use of *ad hoc* modeling of the coronal structure. Methods include static-SRT (Frazin, 2000; Frazin and Janzen, 2002), which assume a static corona, as well as time-dependent ones based on different approaches such as Kalman-filtering (Butala et al., 2010) and temporal-regularization (Vibert et al., 2016). Extensive reviews on the development of SRT, as well as its technical details, can be found in those works and references therein.

SRT currently constitutes the only observational technique able of providing an empirical model-free 3D description of the coronal structure at a global scale. As such, it is of great relevance to the continued development and validation of state-of-the-art 3D magnetohydrodynamical (MHD) models of the solar corona and solar wind (Vásquez, 2016; Lloveras et al., 2020).

Existing SRT studies using VL images are based on data provided by (either ground based or space-borne) coronagraphs in ≈ 1 au circular orbits around the Sun. With the new generation of solar observatories in highly eccentric orbits carrying VL telescopes, namely the Parker Solar Probe (PSP) and the Solar Orbiter (SolO, Müller et al. 2020; García Marirrodriga et al. 2021) missions, new opportunities arise for development and application of tomographic techniques. Vásquez et al. (2019) recently investigated the use of images provided by the PSP Wide-field Imager (WISPR) instrument to carry out tomography of the solar corona.

The SolO Metis coronagraph (Antonucci et al., 2020) records both ultraviolet Lyman-α and VL polarized brightness (pB) full-Sun images of the solar corona. Independently of the main observational windows of Metis (Antonucci et al., 2020), specific orbital segments over which Metis will observe in full-resolution and high cadence, a continuous synoptic observational program will be implemented. This work explores the utility of such a program in terms of using its pB-images for tomographic reconstruction of the 3D distribution of the electron density of the global solar corona.

This study is motivated by the highly eccentric orbit of SolO and its changing latitudinal vantage point. The changing SolO-Sun distance D implies that the radial field of view (FoV) of Metis will continuously vary, and so will do the range of heights that can be reconstructed. The changing orbital speed of the spacecraft implies that the time required to observe the corona from enough view angles to constrain the tomographic inversion problem will also vary with time. The changing latitude θ of the vantage point of Metis also imposes restrictions, as with increasing latitude the line-of-sights (LOSs) associated to the images miss an increasing fraction of the volume of the solar corona.

This work applies the strategy of Vásquez et al. (2019), which explored the use of PSP/WISPR images for tomography. Using the predictive orbital information of SolO and the specifications of the Metis instrument, synthetic Metis pB-images were computed based on 3D MHD simulations of the solar corona. The data was then used to attempt tomographic reconstructions of the models. As this study focuses on assessing what is the impact of the complex geometry of the Metis observations in tomographic reconstructions, steady state simulations were used not to introduce dynamics-induced artifacts. In order to asses how the different geometric aspects of the observations constrain the capacity of doing tomography, images were synthesized from three orbital locations corresponding to extreme geometrical conditions of observation by Metis. To investigate the quality of the reconstructions upon coronal complexity, the three numerical experiments were implemented for two Carrington rotations (CRs), selected from a solar minimum and maximum, respectively.

2. Methodology

2.1. 3D MHD Model of the Solar Corona

The Alfvén Wave Solar atmosphere Model (AWSoM, Sokolov et al. 2013, van der Holst et al. 2014), within the Space-Weather Modeling Framework (SWMF[1]), was used in this work to simulate the solar corona. The single input data that drives the AWSoM model is a synoptic magnetogram, used to set the radial component of the magnetic field (B_r) and the Alfvén wave energy flux at the inner boundary, which corresponds to the upper chromosphere. For the simulations of this work, maps of the Global Oscillation Network Group (GONG) were used, with application of the Air Force Data Assimilation Photospheric Flux Transport model (ADAPT, Arge et al. 2013). The ADAPT-GONG maps provide a physics-based description of the unobserved polar magnetic fields by incorporating large-scale flux transport processes including differential rotation, meridional flows and super-granular flows.

Steady state AWSoM simulations were run based on ADAPT-GONG maps for two different time periods. To experiment on the simplest possible coronal configuration, CR-2082 (2009, 05 April through 03 May) was selected from the solar cycle (SC) 23/24 solar minimum period[2], when the corona exhibited a strong azimuth symmetry, with an equatorial streamer belt dominating low latitudes and coronal holes (CHs) confined to high latitudes in both hemispheres (Lloveras et al., 2020). To study a highly complex coronal configuration, CR-2152 (2014, 28 June 28 through 25 July) was selected during the peak of the SC 24 solar maximum period, when the corona showed both streamers and CHs at all latitudes (Sachdeva et al., 2021).

2.2. The SolO Orbit and Selected Segments

Three segments of the SolO orbit where selected for simulation. Fig. 1 shows predictive plots of the time evolution of orbital parameters of the SolO mission for its full lifetime. The top panel is a plot of the SolO-Sun distance D, while the bottom panel shows the solar latitude θ of SolO. The three red dots highlight the orbital locations around which simulations were implemented: an aphelion ($D \approx 0.95$ au) and a perihelion ($D \approx 0.29$ au) location, both during year 2023, and a location of maximum solar latitude ($\theta \approx +33°$) during year 2029.

For the three simulated observation sequences, Fig. 2 shows the radial FoV of Metis as a function of time (left panels), as well as the solar latitude of SolO (right panels). From top to bottom, panels show the simulations for the aphelion, the perihelion and the maximum solar latitude locations, respectively. In these examples, the step of the solar longitude of SolO between consecutive observations is set to $\Delta\phi = 12°$. In this way, 16 observations span a total of $\Delta\phi = 180°$, allowing to off-limb observe all coronal longitudes. In each left

---

[1] https://clasp.engin.umich.edu/research/theory-computational-methods/swmf-downloadable-software/

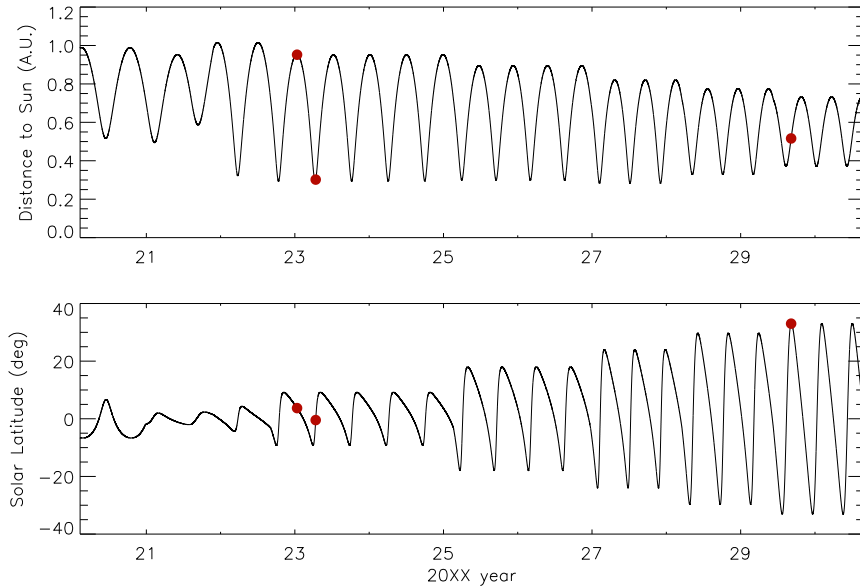[2] https://www.swpc.noaa.gov/products/solar-cycle-progression

Figure 1. SolO orbit. Top panel: time evolution of the SolO-Sun distance. Bottom panel: time evolution of the solar latitude of the disk center as seen by Metis. The three red dots highlight orbital points centered around which data acquisition of Metis is simulated in this work: an aphelion and a perihelion (during year 2023), and a location for which SolO's latitude reaches a maximum value (during year 2029).

panel, the two horizontal dashed lines indicate the limits of the radial FoV that is common to all the images in the full sequence. Within this range of heights, data is then provided by the time series from all its viewing angles.

The locations selected to simulate the image sequences complement each other, representing the different extreme geometrical conditions of observation along the SolO orbit. Around the aphelion ($D \approx 0.95$ au), all images provide approximately the same radial FoV $\approx 5.7 - 10.3$ R$_\odot$. For this first sequence the latitude vantage point is nearly constant and very close to the equator, ranging $\approx +3.0°$ to $+4.5°$. Around the selected perihelion ($D \approx 0.29$ au), the radial FoV changes non-monotonically with the SolO-Sun distance, with the full sequence common FoV being $\approx 2.3 - 3.2$ R$_\odot$. For this second sequence, the latitude of the vantage point increases monotonically, ranging $\approx -9.0°$ to $+7.0°$, still exploring low latitudes. Around the maximum latitude location ($D \approx 0.5$ au), the radial FoV increases monotonically, with the full sequence common FoV being $\approx 3.5 - 5.0$ R$_\odot$. For this third sequence, the latitude is nearly constant, ranging $\approx +30°$ to $+33°$, reaching the maximum latitude to be explored by SolO. Depending on the SolO-Sun distance D, the time gathering period of the sequences taken around the aphelion, perihelion and maximum latitude locations are ≈ 13, 22, and 16 days, respectively.
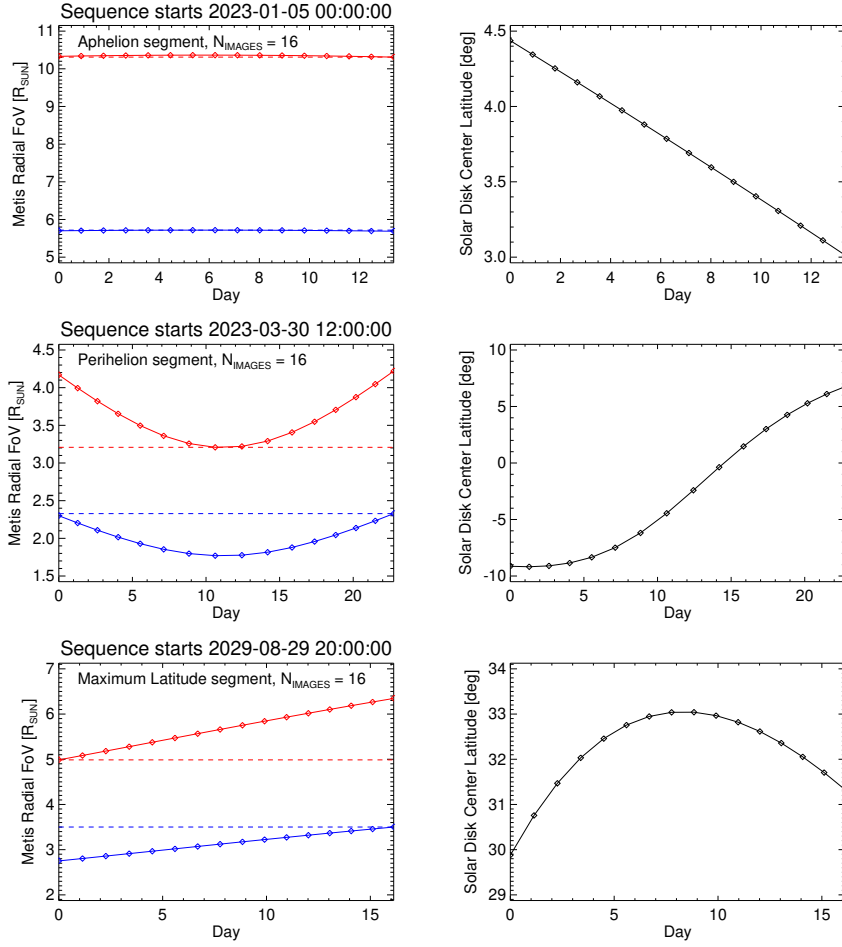
Figure 2. Time evolution of the Metis radial FoV (left panels), and SolO's solar latitude (right panels), for the three time series of simulated observations. The top, middle and bottom panels show the series around the aphelion, perihelion and maximum latitude locations, respectively. In each series, SolO's solar longitude ϕ varies by $\Delta\phi = 12°$ between consecutive observations. In the left panels, for each observing date, the Metis radial FoV extends from the inner radius indicated by the lower blue diamond up to the outer radius indicated by the upper red diamond. The horizontal dashed lines indicate the inner and outer limits of the radial FoV that is common to all the images in the full sequence.

2.3. Metis Synthetic Images

Based on the two AWSoM simulations described in Sec. 2.1, time series of synthetic Metis pB-images of the solar corona were computed for the three orbital segments detailed in Sec 2.2. The images were computed by means of line-of-sight (LOS) integrals of the 3D distribution of the electron density of a model of the solar corona times the appropriate Thomson scattering weighting factor (Minnaert, 1930; van de Hulst, 1950).
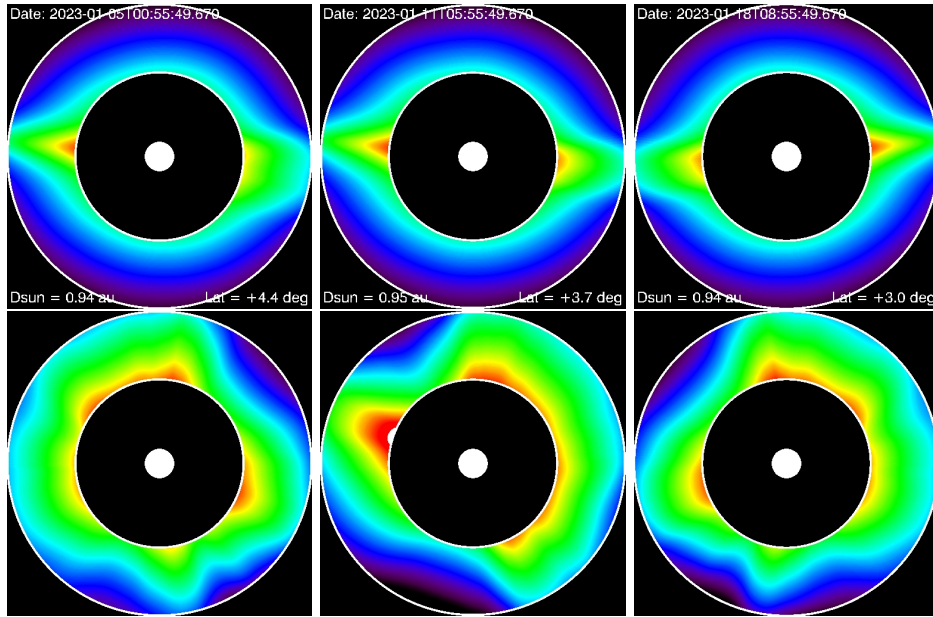
Figure 3. Synthetic Metis *pB*-images (arbitrary units and logarithmic scale) for the aphelion segment, computed from the CR-2082 solar minimum simulation (top panels) and the CR-2152 solar maximum simulation (bottom panels). From left to right the images correspond to the first, middle and last data point of the sequence shown in the top panel of Fig. 2, with top images informing observational date, SolO-Sun distance and solar latitude of SolO. In each image the black circle represents the inner occulter and the white circle the occulted solar disk. The two white rings indicate the boundaries of the radial FoV common to all the images in the sequence, at projected solar radii 5.7 and 10.3 R$_\odot$. For this series, the SolO-Sun distance ranges $\approx 0.94 - 0.95$ au, while SolO's solar latitude ranges $\approx +4.4°$ to $+3.0°$. Note the roughly constant size of the solar disk.

For the aphelion sequence, the first, middle and last images are shown in the left, middle and right panel of Fig. 3, respectively. Top images (which inform relevant ephemeris) correspond to the CR-2082 solar minimum simulation, while bottom ones correspond to the CR-2152 solar maximum simulation. In each image, the two white rings indicate projected solar radii 5.7 and 10.3 R$_\odot$, the boundaries of the radial FoV common to all the images in the sequence. As for this sequence the SolO-Sun distance is roughly constant, so is the radial FoV. Also for this sequence, the solar latitude of SolO is nearly constant and very close to the equator. As a result, the point of view of Metis for the first and last images of the sequence are nearly opposite, so that the resulting images are nearly East/West specular images of each other, for both the CR-2082 and CR-2152 simulations.

For the perihelion sequence, the first, middle and last images are shown in the left, middle and right panel of Fig. 4, respectively. Top images correspond to the CR-2082 solar minimum simulation, while bottom ones correspond to the CR-2152 solar maximum simulation. In each image, the two white rings indicate projected solar radii 2.3 and 3.2 R$_\odot$, the boundaries of the radial FoV common to all the images in the sequence. In this sequence the SolO-Sun distance varies in
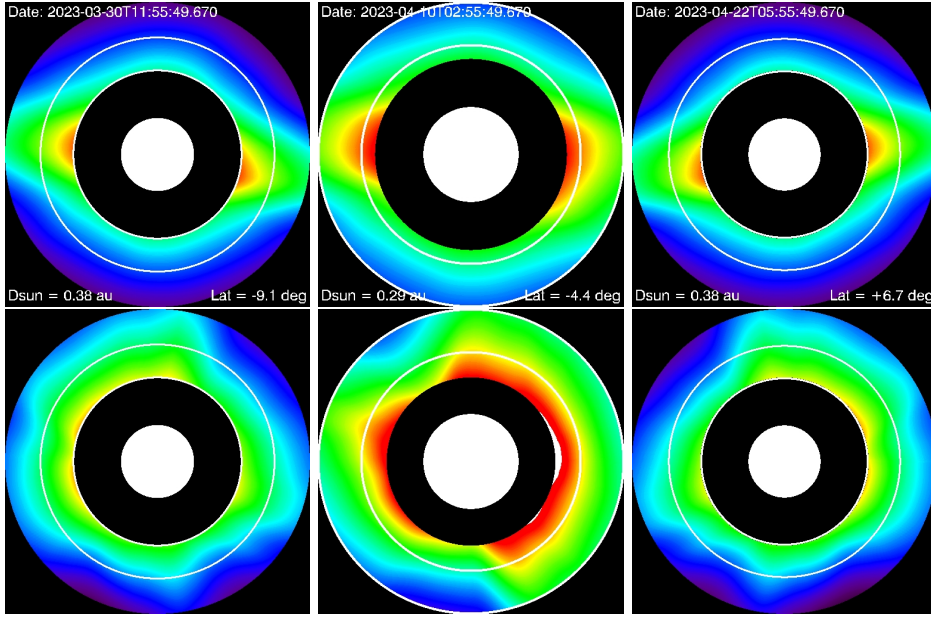
Figure 4. Same as Fig. 3 but for the perihelion segment, for the CR-2082 solar minimum simulation (top panels) and the CR-2152 solar maximum simulation (bottom panels). From left to right the images correspond to the first, middle and last data point of the sequence shown in the middle panel of Fig. 2. The two white rings indicate the boundaries of the radial FoV common to all the images in the sequence, at projected solar radii 2.3 and 3.2 $R_\odot$. For this series, the SolO-Sun distance ranges $\approx 0.38 - 0.29$ au, while SolO's solar latitude ranges $\approx -9.1°$ to $+6.7°$. Note the larger size of the solar disk at perihelion (middle panels).

the range $\approx 0.38 - 0.29$ au. The inner limit of the common radial FoV ($\approx 2.3\ R_\odot$) is imposed by the more distant images (first and last one), while the outer limit of the common radial FoV ($\approx 3.2\ R_\odot$) is imposed by the perihelion (middle) image. SolO's excursion in solar latitude for this series, wider than in the aphelion case, is still limited to rather low latitudes. As the series is centered around perihelion, the first and last images are simulated from the same distance to the Sun. As a result, the first and last image are again nearly East/West specular images of each other, for both the CR-2082 and CR-2152 simulations.

For the maximum solar latitude sequence, the first, middle and last images are shown in the left, middle and right panel of Fig. 5, respectively. Top images correspond to the CR-2082 solar minimum simulation, while bottom ones correspond to the CR-2152 solar maximum simulation. In each image, the two white rings indicate projected solar radii 3.5 and 5.0 $R_\odot$, the boundaries of the radial FoV common to all the images in the sequence. In this sequence the SolO-Sun distance varies in the range $\approx 0.45 - 0.58$ au. The outer limit of the common radial FoV ($\approx 5.0\ R_\odot$) is imposed by the less distant observation (first one), while the outer limit of the common radial FoV ($\approx 3.5\ R_\odot$) is imposed by the more distant observation (last one). For this series, SolO's solar latitude is nearly constant and quite large, so that streamer structures are not observed edge-on
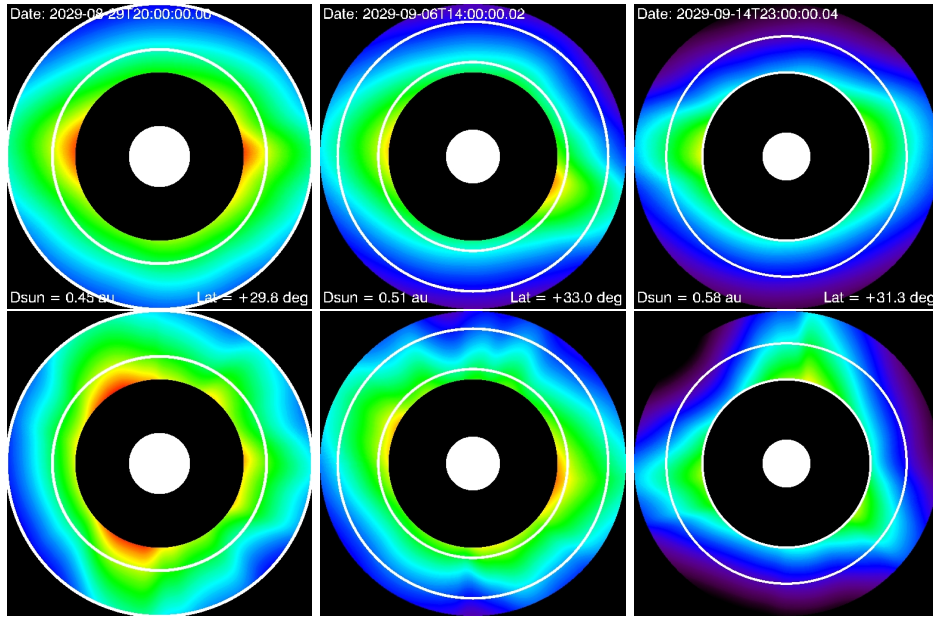
Figure 5. Same as Fig. 3 but for the maximum latitude segment, computed from the CR-2082 solar minimum simulation (top panels) and the CR-2152 solar maximum simulation (bottom panels). From left to right the images correspond to the first, middle and last data point of the sequence shown in the bottom panel of Fig. 2. The two white rings indicate the boundaries of the radial FoV common to all the images in the sequence, at projected solar radii 3.5 and 5.0 $R_\odot$. For this series, the SolO-Sun distance ranges $\approx 0.45 - 0.58$ au, while SolO's solar latitude ranges $\approx +29.8°$ to $+33.0°$. Note the decreasing size of the solar disk with increasing distance.

as in the previous two cases. As a result, these images exhibit less prominent and wider streamers, and are characterized by a smaller dynamic range.

2.4. SRT, Computational Grid, and Image Size

SRT uses a time series of coronal images (taken on a wavelength for which the corona is optically thin) to pose a linear inversion problem. The combination of the solar rotation and the orbital motion of the observer provide the required view angles. Each image in the series is a 2D projection of an underlying 3D emissivity structure. The intensity registered by a single pixel is the result of a LOS integral of the coronal emissivity. In the case of VL pB-images, this emissivity is proportional to the coronal electron density times a known geometrical factor. The intensity values of each pixel of every image in the time series are arranged as a very large column vector of M brightness measurements. By discretizing the coronal volume in N cells, each LOS integral is expressed as a discrete sum of the known geometric scattering weighting factor evaluated at each computational cell threaded by the LOS, times the unknown electron density in the respective cells. The column data vector of M intensities is then equaled to a very large $M \times N$ sparse projection matrix (containing only known factors depending on the observational geometry) multiplied by a column vector

whose N elements are the unknown values of the coronal electron density in each cell of the computational grid. The non-squared sparse projection matrix is non-invertible. The linear inversion problem is then posed as a multi-dimensional optimization problem, in which there are N unknowns. In inverting for the electron density, the SRT solution is subject to 3D spatial regularization, to suppress spurious high-frequency artifacts (Frazin et al., 2007). In this work, the technique originally developed by Frazin (2000) and further developed by Frazin, Vásquez, and Kamalabadi (2009) is used. For detailed discussions on SRT the reader is referred to references provided in Sec. 1.

While the VL detector of Metis has a size of 2048^2 pixels, the synoptic program is to be implemented with a lower resolution of 512^2. This 16-fold binning, necessary to be able to continuously take images with a cadence of a few images per day, will also improve the signal-to-noise of the images. In the simulations of this work the synthetic images were computed at this resolution.

To treat the tomographic problem the coronal volume is discretized on a uniform spherical grid, with radial cell size Δr, and equal latitudinal $\Delta \theta$ and azimuth cell size $\Delta \phi$. The specific size of the radial and angular cell size were set in relation to the number of pixels in the images and the radial field of view of each case, as detailed next. The characteristic grid cell size described below is what is currently applied in routine fashion in carrying out tomography based on data provided by the Large Angle and Spectrometric COronagraph (LASCO) C2 instrument, on board the Solar and Heliospheric Observatory (SoHO), whose FoV covers heights comparable to those of Metis in its different orbital locations.

In the aphelion case, the full FoV linear size is $L \approx 20.7\,\mathrm{R}_\odot$, with linear pixel size $d \approx 0.04\,\mathrm{R}_\odot$. The tomographic cell size was set to $\Delta r = 0.2\,\mathrm{R}_\odot$ and $\Delta \theta = 2°$. As the common radial FoV ranges $5.7 - 10.3\,\mathrm{R}_\odot$, the average radial cell is located at height $\langle r \rangle = 8.0\,\mathrm{R}_\odot$, with average angular linear size $\langle \Delta l \rangle = \langle r \rangle \times \Delta \theta \approx 0.3\,\mathrm{R}_\odot$. In this way, the choice of grid size provides an average cell of linear dimensions $\approx 0.2 \times 0.3\,\mathrm{R}_\odot$. Comparing that to the linear pixel size, note that such a cell in the plane-of-the-sky is threaded by $\Delta r \times \langle \Delta l \rangle / d^2 \approx 38$ LOSs. Every LOS is numerically treated individually, and then a 16-fold binning is applied, so that the average cell is threaded by two 16-binned LOSs.

In the perihelion case, the full FoV linear size changes, with an average size $\langle L \rangle \approx 7.3\,\mathrm{R}_\odot$, and a linear pixel size $d \approx 0.014\,\mathrm{R}_\odot$. The tomographic cell size was set to $\Delta r = 0.1\,\mathrm{R}_\odot$ and $\Delta \theta = 2°$. As in this case the common radial FoV ranges $2.3 - 3.2\,\mathrm{R}_\odot$, the average radial cell is located at height $\langle r \rangle = 2.75\,\mathrm{R}_\odot$, and its angular linear size then $\langle \Delta l \rangle \approx 0.1\,\mathrm{R}_\odot$. In the plane-of-the-sky such cell is threaded by ≈ 51 LOSs. Again, a 16-fold binning is applied, so that the average cell is effectively threaded by three 16-binned LOSs.

In the maximum latitude case, the full FoV linear size also changes, with an average size $\langle L \rangle \approx 11.4\,\mathrm{R}_\odot$, and a linear pixel size $d \approx 0.022\,\mathrm{R}_\odot$. The tomographic cell size was set to $\Delta r = 0.1\,\mathrm{R}_\odot$ and $\Delta \theta = 2°$. As in this case the common radial FoV ranges $3.5 - 5.0\,\mathrm{R}_\odot$, the average radial cell is located at height $\langle r \rangle = 4.25\,\mathrm{R}_\odot$, and its angular linear size then $\langle \Delta l \rangle \approx 0.15\,\mathrm{R}_\odot$. In the plane-of-the-sky such cell is threaded by ≈ 31 LOSs. Again, a 16-fold binning is applied, so that the average cell is effectively threaded by two 16-binned LOSs.
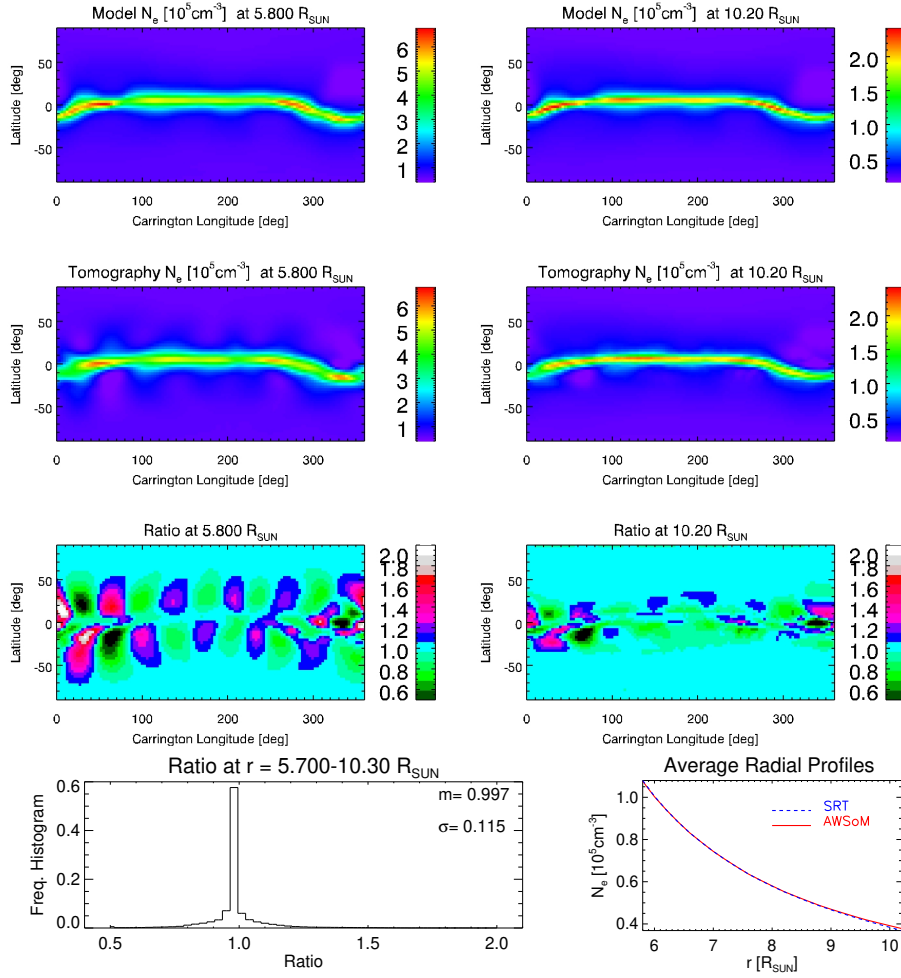
Figure 6. Comparison of the CR-2082 solar minimum simulation and its tomographic reconstruction for the aphelion segment. Maps are shown at heights 5.8 $R_\odot$ (left panels) and 10.2 $R_\odot$ (right panels). Top panels: latitude/longitude maps of the electron density N_e of the model. Second row of panels: maps of N_e given by the tomographic reconstruction. Third row of panels: maps of the ratio between N_e of the tomographic reconstruction and of the model. Bottom-left panel: frequency histogram of the reconstruction-to-model electron density ratio for the full reconstructed volume. The median m and standard deviation σ are indicated. Bottom-right panel: $N_e(r)$ averaged over all latitudes and longitudes for the model (solid-red) and the reconstruction (dashed-blue).

3. Results

Tomographic reconstruction of the electron density of the two AWSoM simulations were implemented based on the image series synthesized around each of the three selected orbital segments, for a total of six reconstructions. In carrying out each reconstruction, two different values of the longitudinal step between
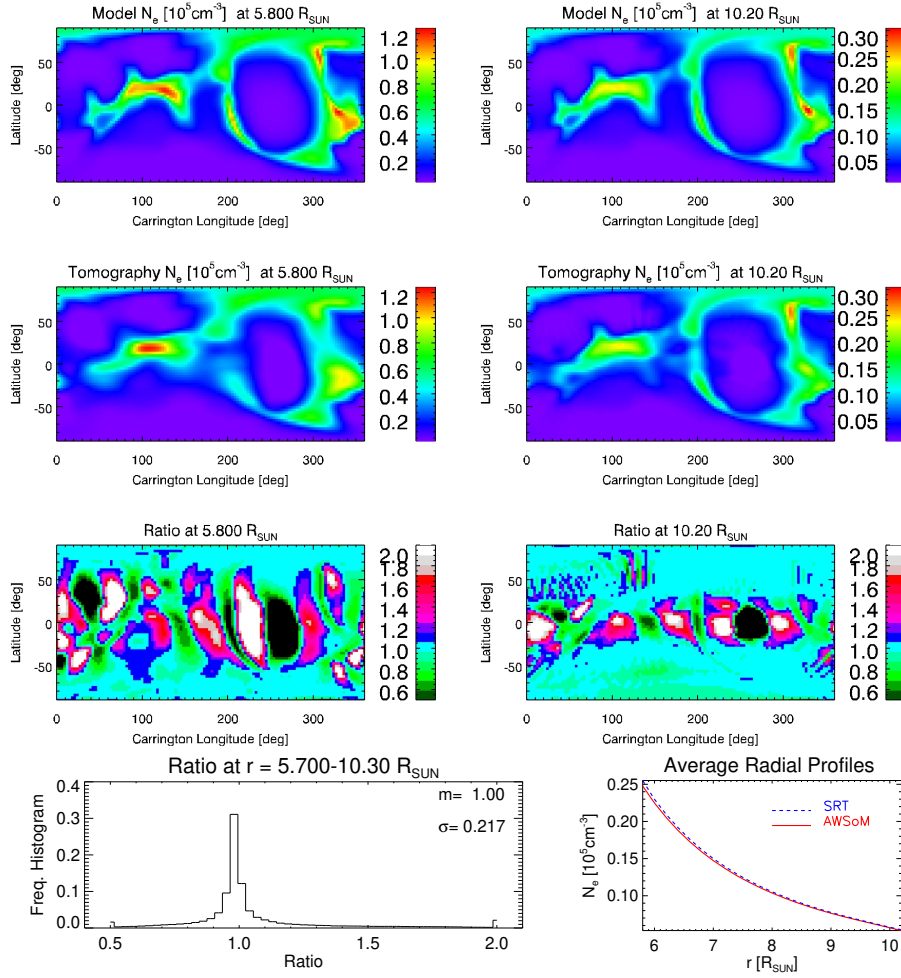
Figure 7. Same as Fig. 6 but for the CR-2152 solar maximum simulation.

consecutive observations were experimented, $\Delta\phi = 12°$ and $6°$. The larger value was found to be optimal for the solar minimum corona experiments, while the smaller one is optimal for the solar maximum experiments. Results of the six reconstructions are reported next, each case using the optimal longitude step.

3.1. Tomographic Reconstruction from Aphelion

For this orbital segment, tomographic reconstruction of the two AWSoM simulations was carried out over the radial FoV $\approx 5.7 - 10.3$ $R_\odot$ common to all images in the series (Fig. 2, top-left panel). Results for the solar minimum and maximum simulations are shown in Figs. 6 and 7, respectively. In both figures (from top to bottom), the first row of panels shows latitude/longitude maps of the electron density of the corresponding AWSoM model at heliocentric heights
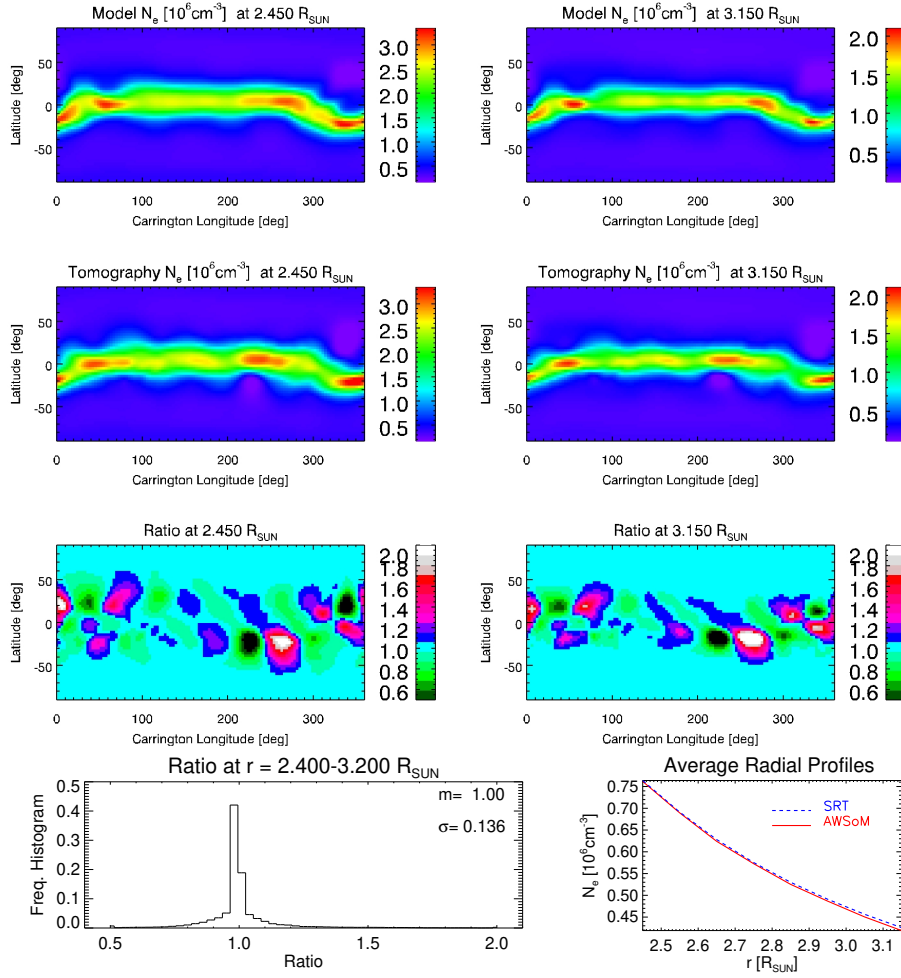
Figure 8. Comparison of the CR-2082 solar minimum simulation and its tomographic reconstruction for the perihelion segment at sample heights 2.45 R$_\odot$ and 3.15 R$_\odot$ (top three rows of panels), and for the whole reconstructed volume (bottom row of panels).

5.8 R$_\odot$ (left panel) and 10.2 R$_\odot$ (right panel), near the lowest and largest height covered by the data. The second row of panels shows the corresponding maps of the tomographicaly reconstructed electron density. The third row of panels shows maps of the ratio between the electron density of the tomographic reconstruction and that of the model. The bottom-left panel shows the frequency histogram of the reconstruction-to-model electron density ratio, for the whole reconstructed coronal volume.

For the two simulations, the histogram exhibits a median value ≈ 1, with standard deviation ≈ 12% and ≈ 22% for the solar minimum and maximum models, respectively. The larger deviation in the case of the more complex corona is expected due to the richer small-scale structure, whose reconstruction
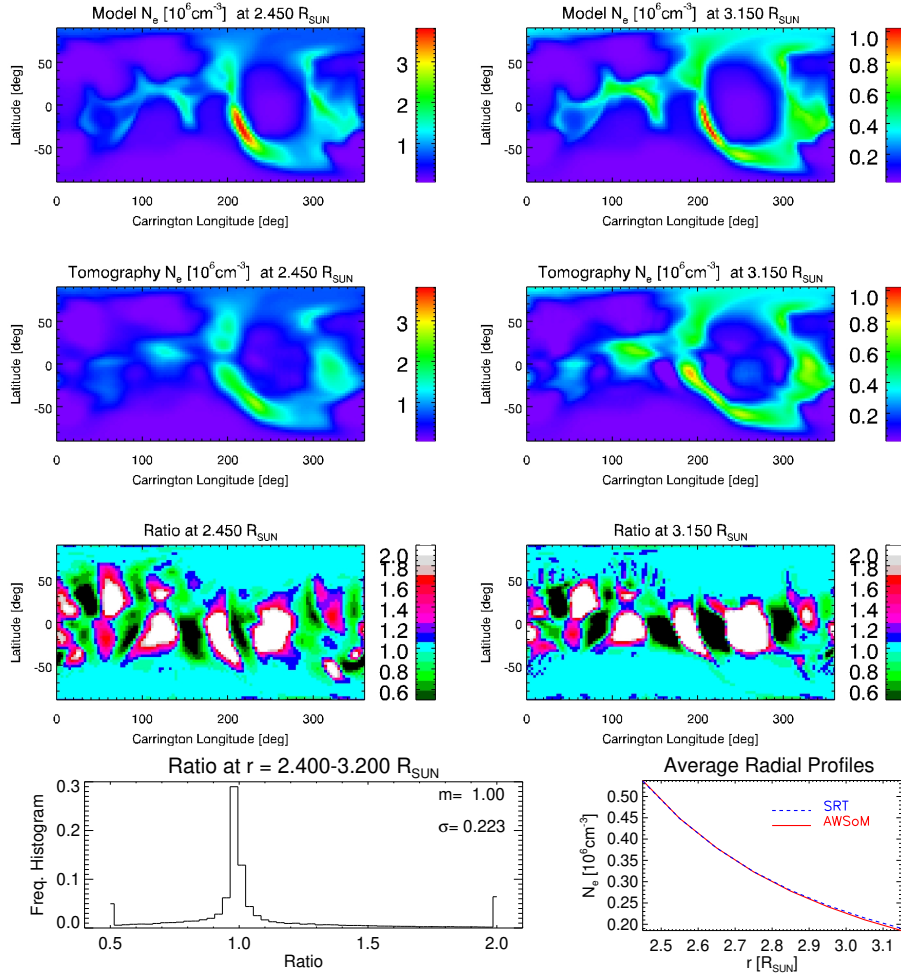
Figure 9. Same as Fig. 8 but for the CR-2152 solar maximum simulation.

is compromised by the regularization scheme. The bottom-right panel shows the global average radial trend of the electron density, which is well reproduced by the tomographic reconstruction of both simulations.

3.2. Tomographic Reconstruction from Perihelion

For this orbital segment, tomographic reconstruction of the two AWSoM simulations was carried over the radial FoV $\approx 2.3 - 3.2$ $R_\odot$ common to all images in the series (Fig. 2, middle-left panel), although all the available data was used in constraining the inversion problem (inlcuding pixels outside the common FoV). Results for the solar minimum and maximum simulations are shown in Figs. 8 and 9, respectively. In both figures, results are shown at heliocentric heights 2.45 $R_\odot$ and 3.15 $R_\odot$, near (and within) the lowest and largest height of the
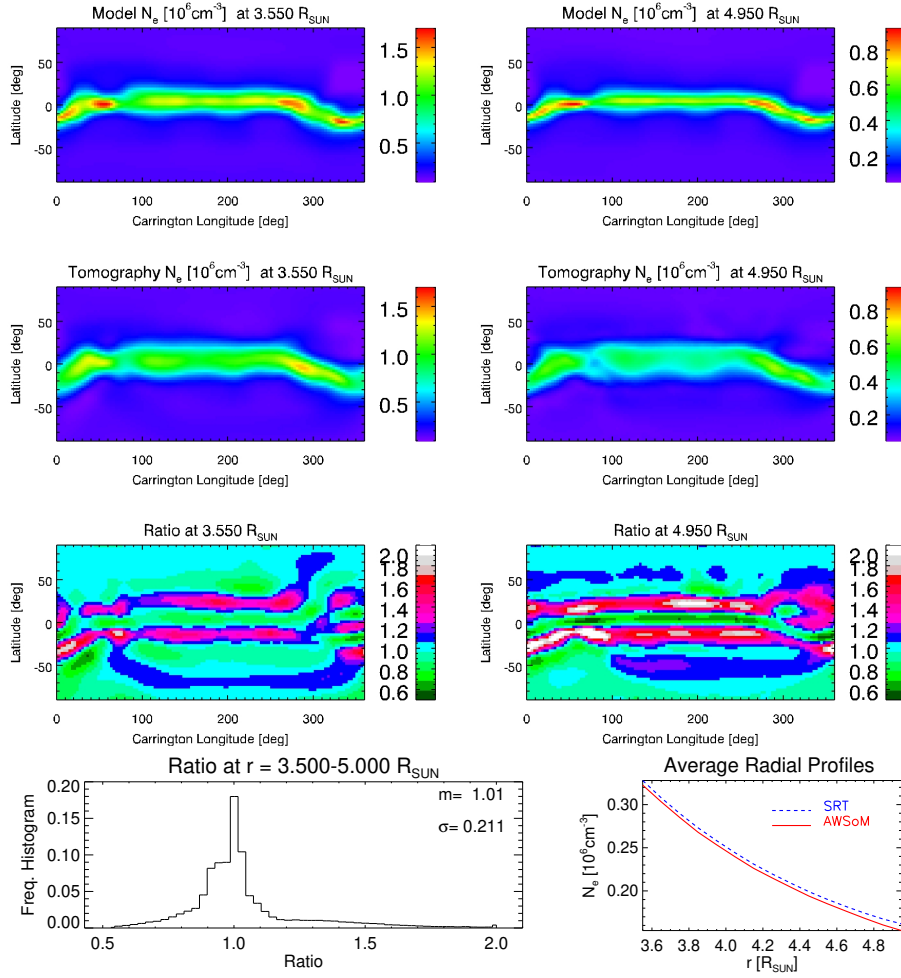
Figure 10. Comparison of the CR-2082 solar minimum simulation and its tomographic reconstruction for the maximum latitude segment, at sample heights 3.55 R$_\odot$ and 4.95 R$_\odot$ (top three rows of panels), and for the whole reconstructed volume (bottom row of panels).

reconstructed range of heights. Being based again on observations simulated from low latitudes, the accuracy of the tomographic reconstruction for the perihelion segment is comparable to the aphelion case. For both models, the global histogram of the recontruction-to-model electron density ratio again exhibits a median value ≈ 1, with standard deviation $\approx 14\%$ and $\approx 22\%$ for the solar minimum and maximum models, respectively. The global average radial trend of the electron density is again well reproduced by the tomographic reconstruction of both simulations.
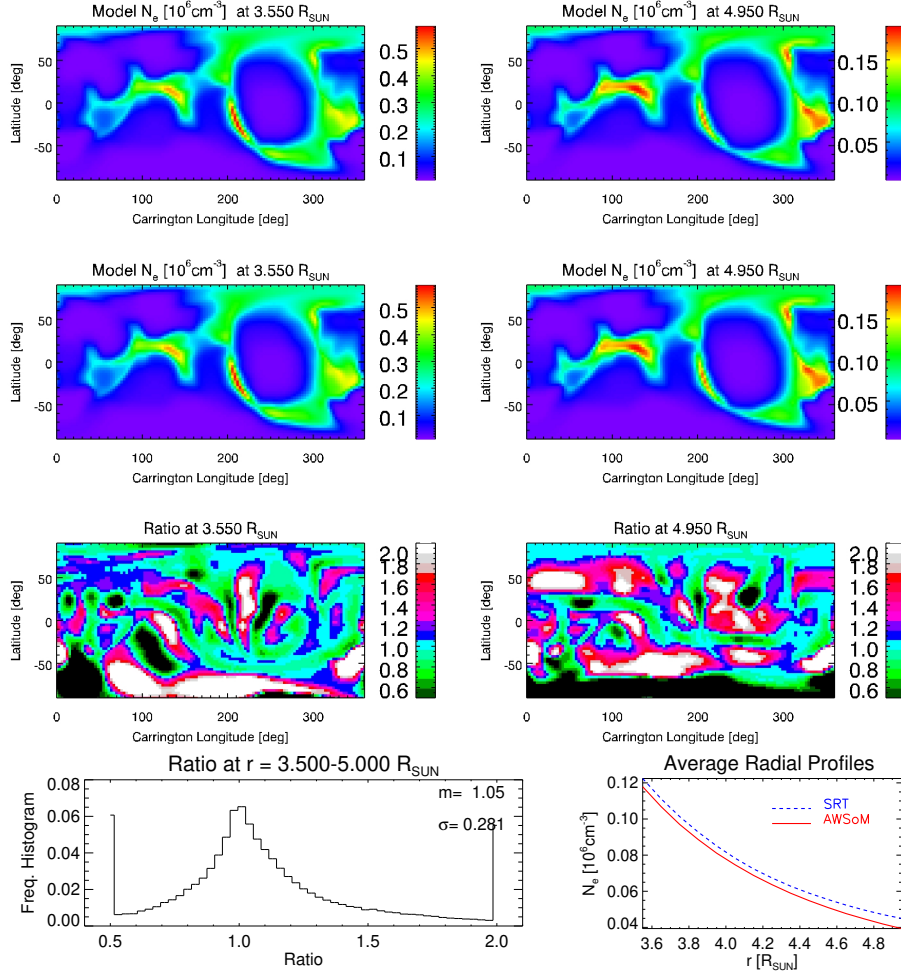
Figure 11. Same as Fig. 10 but for the CR-2152 solar maximum simulation.

3.3. Tomographic Reconstruction from Maximum Solar Latitude

For this orbital segment, tomographic reconstruction of the two AWSoM simulations was carried over the radial FoV $\approx 3.5 - 5.0$ R$_\odot$ common to all images in the series (Fig. 2, bottom-left panel), although all the available data was used (as in the case of the perihelion segment). Results for the solar minimum and maximum simulations are shown in Figs. 10 and 11, respectively. In both figures, results are shown at heliocentric heights 3.55 R$_\odot$ and 4.95 R$_\odot$, near (and within) the lowest and largest height of the reconstructed range of heights.

Being based on observations simulated from a (nearly constant) high latitude $\theta \approx +32°$, the accuracy of the tomographic reconstruction for the solar maximum latitude segment is comparatively less accurate than for both the aphelion and perihelion cases. Note how in the case of the solar maximum simulation, the

reconstruction fails for the range of latitudes $\approx -90°$ to $\approx -50°$, a region largely non-accessed by the LOSs of the observational sequence, due to the high (positive) latitude location of the spacecraft. Interestingly enough, the reconstruction of the solar minimum simulation is not particularly unaccurate over that same latitude range. This is due to a combination of the corona being much simpler (in particular lacking small scale structure at high latitudes) and the tomography spatial regularization scheme.

The global histogram of the reconstruction-to-model electron density ratio exhibits a median value ≈ 1.01 for the solar minimum simulation and ≈ 1.05 for the solar maximum simulation. Also, for each simulation the standard deviation of the ratio histogram is the largest of the three orbital segments, being $\approx 21\%$ and $\approx 28\%$ for the solar minimum and maximum simulations, respectively. Likewise, the global average radial trend of the electron density departs from the model in noticeable fashion (unlike in the aphelion and perihelion segments), with the difference being larger in the case of the solar maximum simulation.

4. Conclusions and Discussion

This work explored the use of pB-images taken by a continuous synoptic program of observations of Metis to carry out tomographic reconstructions of the 3D distribution of the electron density of the solar corona. Based on steady state 3D MHD simulations of the solar corona, and the orbital information of SolO, time series of Metis pB-images were synthesized and used for tomographic reconstruction of the electron density of the model. Images were synthesized from three selected locations along the SolO orbit: aphelion, perihelion and maximum solar latitude, representing extreme geometrical conditions of observation by Metis. To experiment with both simple and complex coronal structure, the three image sequences were synthesized based on two simulations of the solar corona, corresponding to a solar minimum and a solar maximum rotation. The main conclusions of this study are summarized next.

- Aphelion segment: the image sequence is obtained over a period of $\approx$ 13 days, and the range of heights over which the electron density can be reconstructed is $\approx 5.7 - 10.3$ R$_\odot$.
- Perihelion segment: the image sequence is obtained over a period of $\approx$ 22 days, and the range of heights over which the electron density can be reconstructed is is $\approx 2.3 - 3.2$ R$_\odot$.
- For orbital segments in between aphelion and perihelion, the data gathering period and the range of heights over which the density can be reconstructed are intermediate to the results informed above (see next point as example).
- Maximum solar latitude segment: the image sequence is obtained over a period of $\approx$ 16 days, and the range of heights over which the electron density can be reconstructed is is $\approx 3.5 - 5.0$ R$_\odot$.
- Observing from low solar latitude locations, such as the aphelion and perihelion segments explored in this work, the tomographic reconstruction is highly successful for both the solar minimum and maximum simulations.

- Observing from larger solar latitude locations, such as the maximum solar latitude segment explored in this work, tomographic reconstruction is unfeasible over the high latitudes of the hemisphere opposite to the location of SolO. Even so, a large fraction of the coronal volume can be satisfactorily reconstructed in this case.
- In the case of a simple dipolar corona, tomographic reconstructions required consecutive images taken from locations separated by a solar longitude step $\Delta\phi = 12°$. In the case of a highly complex corona, the solar longitude step was reduced to $\Delta\phi = 6°$ to achieve satisfactory results.
- The observational cadence in these simulations ranges from ≈ 0.7 images/day (perihelion segment) to ≈ 1.2 images/day (aphelion segment), for the solar minimum experiment. In the case of the solar maximum experiment, the optimal cadence values are twice as large, ranging $\approx 1.4 - 2.4$ images/day.

The cadence values found in this study to be optimal for tomography with Metis can be approximately replicated at any point of the SolO orbit with a synoptic program providing at least 4 images/day. This is well within the capability of the current Metis synoptic program, performing synoptic observations with a $2 - 3$ hr cadence, allowing for experimentation with other cadence values as well. This current program will also provide data redundancy (useful for validation of tomographic reconstructions). Its cadence will also provide continuous opportunity to select images avoiding highly dynamic events, which compromise the accuracy of tomographic reconstructions.

This study was based on steady-state simulations, so that the reconstructions were not affected by dynamics-induced artifacts. In dealing with actual Metis data, the optimal observational cadence for a specific period of interest will also depend on the observed level of coronal dynamics, and various cadence values will be experimented. Previous experience implementing tomography with LASCO-C2 data indicates that 1 image/day (implying $\Delta\phi \approx 13°$ for LASCO-C2) is around optimal (P. Lamy, private communication). In the case of actual data, the perihelion case will likely be more difficult to tackle than the aphelion case, because the data acquisition time is longer and the corona is more highly structured at lower heights.

The varying degree of dynamical evolution exhibited by the solar corona during the $13 - 22$ day data acquisition period required for tomography with Metis at different segments along the orbit of SolO, will introduce artifacts in the reconstructions in the form of unreconstructed regions dubbed "zero-density-artifacts" (ZDAs) (Frazin, 2000; Frazin and Janzen, 2002). These can be mitigated using time-dependent tomographic reconstruction schemes, and also by partial masking of the images (Butala et al., 2010; Vibert et al., 2016). Different approaches will be experimented with actual images in order to asses how dynamics-induced artifacts can be best handled in the case of Metis observations.

Another approach to mitigate ZDAs in reconstructions of the solar corona, that has not been explored so far, is to resort to the approach of neural network algorithms. Training such a neural network will require constructing a large data base of simulated data pairs of known time-evolving models (with varying degrees

of dynamics) and their reconstructions based on synthetic images. This novel approach will be explored in the future for tomography with VL instruments, such as Metis and LASCO-C2, as well as for EUV tomography.

Besides the specific solar physics interest of tomographic reconstructions of the solar corona in general, there is also a side technical benefit from implementing reconstructions with data provided by Metis at any suitable opportunity. Along most of the SolO orbit, the radial FoV of Metis overlaps with that of pre-existing and still operative space-borne VL coronagraphs, such as SoHO/LASCO-C2 and STEREO-A/COR1-2 (Frazin et al., 2012). Despite their different observational view angles, a statistical comparison of the results of independent and simultaneous tomographic reconstructions of the coronal electron density based on images from different instruments can be used as an inter-calibration tool among them.

As a closing comment, we plan to combine VL tomography with tomography based on Metis H I Lyman-α images. This will in principle allow 3D mapping of the Lyman-α Doppler dimming factor. Those results could then be inverted to compute 3D maps of the solar wind velocity (Bemporad et al., 2021; Romoli et al., 2021). This project will be focus of a next effort.

Disclosure of Potential Conflicts of Interest

The authors declare that they have no conflicts of interest.

References

Antonucci, E., Romoli, M., Andretta, V., Fineschi, S., Heinzel, P., Moses, J.D., Naletto, G., Nicolini, G., Spadaro, D., Teriaca, L., Berlicki, A., Capobianco, G., Crescenzio, G., Da Deppo, V., Focardi, M., Frassetto, F., Heerlein, K., Landini, F., Magli, E., Marco Malvezzi, A., Massone, G., Melich, R., Nicolosi, P., Noci, G., Pancrazzi, M., Pelizzo, M.G., Poletto, L., Sasso, C., Schühle, U., Solanki, S.K., Strachan, L., Susino, R., Tondello, G., Uslenghi, M., Woch, J., Abbo, L., Bemporad, A., Casti, M., Dolei, S., Grimani, C., Messerotti, M., Ricci, M., Straus, T., Telloni, D., Zuppella, P., Auchère, F., Bruno, R., Ciaravella, A., Corso, A.J., Alvarez Copano, M., Aznar Cuadrado, R., D'Amicis, R., Enge, R., Gravina, A., Jejčič, S., Lamy, P., Lanzafame, A., Meierdierks, T., Papagiannaki, I., Peter, H., Fernandez Rico, G., Giday Sertsu, M., Staub, J., Tsinganos, K., Velli, M., Ventura, R., Verroi, E., Vial, J.-C., Vives, S., Volpicelli, A., Werner, S., Zerr, A., Negri, B., Castronuovo, M., Gabrielli,

A., Bertacin, R., Carpentiero, R., Natalucci, S., Marliani, F., Cesa, M., Laget, P., Morea, D., Pieraccini, S., Radaelli, P., Sandri, P., Sarra, P., Cesare, S., Del Forno, F., Massa, E., Montabone, M., Mottini, S., Quattropani, D., Schillaci, T., Boccardo, R., Brando, R., Pandi, A., Baietto, C., Bertone, R., Alvarez-Herrero, A., García Parejo, P., Cebollero, M., Amoruso, M., Centonze, V.: 2020, Metis: the Solar Orbiter visible light and ultraviolet coronal imager. *Astron. Astrophys.* **642**, A10. DOI. ADS.

Arge, C.N., Henney, C.J., Hernandez, I.G., Toussaint, W.A., Koller, J., Godinez, H.C.: 2013, Modeling the corona and solar wind using ADAPT maps that include far-side observations. **1539**, 11. DOI. ADS.

Bemporad, A., Giordano, S., Zangrilli, L., Frassati, F.: 2021, Combining White Light and UV Lyman-alpha Coronagraphic Images to determine the Solar Wind Speed: the Quick Inversion Method. *arXiv e-prints*, arXiv:2107.06811. ADS.

Butala, M.D., Hewett, R.J., Frazin, R.A., Kamalabadi, F.: 2010, Dynamic Three-Dimensional Tomography of the Solar Corona. *Solar Phys.* **262**, 495. DOI. ADS.

Frazin, R.A.: 2000, Tomography of the Solar Corona. I. A Robust, Regularized, Positive Estimation Method. *Astrophys. J.* **530**, 1026. DOI. ADS.

Frazin, R.A., Janzen, P.: 2002, Tomography of the Solar Corona. II. Robust, Regularized, Positive Estimation of the Three-dimensional Electron Density Distribution from LASCO-C2 Polarized White-Light Images. *Astrophys. J.* **570**, 408. DOI. ADS.

Frazin, R.A., Vásquez, A.M., Kamalabadi, F.: 2009, Quantitative, Three-dimensional Analysis of the Global Corona with Multi-spacecraft Differential Emission Measure Tomography. *Astrophys. J.* **701**, 547. DOI. ADS.

Frazin, R.A., Vásquez, A.M., Kamalabadi, F., Park, H.: 2007, Three-dimensional Tomographic Analysis of a High-Cadence LASCO-C2 Polarized Brightness Sequence. *Astrophys. J. Lett.* **671**, L201. DOI. ADS.

Frazin, R.A., Vásquez, A.M., Thompson, W.T., Hewett, R.J., Lamy, P., Llebaria, A., Vourlidas, A., Burkepile, J.: 2012, Intercomparison of the LASCO-C2, SECCHI-COR1, SECCHI-COR2, and Mk4 Coronagraphs. *Solar Phys.* **280**, 273. DOI. ADS.

García Marirrodriga, C., Pacros, A., Strandmoe, S., Arcioni, M., Arts, A., Ashcroft, C., Ayache, L., Bonnefous, Y., Brahimi, N., Cipriani, F., Damasio, C., De Jong, P., Déprez, G., Fahmy, S., Fels, R., Fiebrich, J., Hass, C., Hernández, C., Icardi, L., Junge, A., Kletzkine, P., Laget, P., Le Deuff, Y., Liebold, F., Lodiot, S., Marliani, F., Mascarello, M., Müller, D., Oganessian, A., Olivier, P., Palombo, E., Philippe, C., Ragnit, U., Ramachandran, J., Sánchez Pérez, J.M., Stienstra, M.M., Thürey, S., Urwin, A., Wirth, K., Zouganelis, I.: 2021, Solar Orbiter: Mission and spacecraft design. *Astron. Astrophys.* **646**, A121. DOI. ADS.

Lloveras, D.G., Vásquez, A.M., Nuevo, F.A., Mac Cormack, C., Sachdeva, N., Manchester, W., Van der Holst, B., Frazin, R.A.: 2020, Thermodynamic Structure of the Solar Corona: Tomographic Reconstructions and MHD Modeling. *Solar Phys.* **295**, 76. DOI. ADS.

Minnaert, M.: 1930, On the continuous spectrum of the corona and its polarisation. With 3 figures. (Received July 30, 1930). *Zeits. Astrophys.* **1**, 209. ADS.

Müller, D., St. Cyr, O.C., Zouganelis, I., Gilbert, H.R., Marsden, R., Nieves-Chinchilla, T., Antonucci, E., Auchère, F., Berghmans, D., Horbury, T.S., Howard, R.A., Krucker, S., Maksimovic, M., Owen, C.J., Rochus, P., Rodriguez-Pacheco, J., Romoli, M., Solanki, S.K., Bruno, R., Carlsson, M., Fludra, A., Harra, L., Hassler, D.M., Livi, S., Louarn, P., Peter, H., Schühle, U., Teriaca, L., del Toro Iniesta, J.C., Wimmer-Schweingruber, R.F., Marsch, E., Velli, M., De Groof, A., Walsh, A., Williams, D.: 2020, The Solar Orbiter mission. Science overview. *Astron. Astrophys.* **642**, A1. DOI. ADS.

Romoli, M., Antonucci, E., Andretta, V., Capuano, G.E., Da Deppo, V., De Leo, Y., Downs, C., Fineschi, S., Heinzel, P., Landini, F., Liberatore, A., Naletto, G., Nicolini, G., Pancrazzi, M., Sasso, C., Spadaro, D., Susino, R., Telloni, D., Teriaca, L., Uslenghi, M., Wang, Y.M., Bemporad, A., Capobianco, G., Casti, M., Fabi, M., Frassati, F., Frassetto, F., Giordano, S., Grimani, C., Jerse, G., Magli, E., Massone, G., Messerotti, M., Moses, D., Pelizzo, M.G., Romano, P., Schühle, U., Slemer, A., Stangalini, M., Straus, T., Volpicelli, C.A., Zangrilli, L., Zuppella, P., Abbo, L., Auchére, F., Aznar Cuadrado, R., Berlicki, A., Bruno, R., Ciaravella, A., D'Amicis, R., Lamy, P., Lanzafame, A., Malvezzi, A.M., Nicolosi, P., Nisticò, G., Peter, H., Plainaki, C., Poletto, L., Reale, F., Solanki, S.K., Strachan, L., Tondello, G., Tsinganos, K., Velli, M., Ventura, R., Vial, J.C., Woch, J., Zimbardo, G.: 2021, First light observations of the solar wind in the outer corona with the Metis coronagraph. *arXiv e-prints*, arXiv:2106.13344. ADS.

Sachdeva, N., Tóth, G., Manchester, W.B., van der Holst, B., Huang, Z., Sokolov, I.V., Zhao, L., Shidi, Q.A., Chen, Y., Gombosi, T.I., Henney, C.J., Lloveras, D.G., Vásquez, A.M.:

2021, Simulating Solar Maximum Conditions Using the Alfvén Wave Solar Atmosphere Model (AWSoM). *Astrophys. J.* **923**, 176. DOI. ADS.

Sokolov, I.V., van der Holst, B., Oran, R., Downs, C., Roussev, I.I., Jin, M., Manchester, I. Ward B., Evans, R.M., Gombosi, T.I.: 2013, Magnetohydrodynamic Waves and Coronal Heating: Unifying Empirical and MHD Turbulence Models. *Astrophys. J.* **764**, 23. DOI. ADS.

van de Hulst, H.C.: 1950, The electron density of the solar corona. *Bull. Astronom. Instit. Netherlands* **11**, 135. ADS.

van der Holst, B., Sokolov, I.V., Meng, X., Jin, M., Manchester, W.B. IV, Tóth, G., Gombosi, T.I.: 2014, Alfvén Wave Solar Model (AWSoM): Coronal Heating. *Astrophys. J.* **782**, 81. DOI. ADS.

Vásquez, A.M.: 2016, Seeing the solar corona in three dimensions. *Advances in Space Research* **57**, 1286. DOI. ADS.

Vásquez, A.M., Frazin, R.A., Vourlidas, A., Manchester, W.B., van der Holst, B., Howard, R.A., Lamy, P.: 2019, Tomography of the Solar Corona with the Wide-Field Imager for the Parker Solar Probe. *Solar Phys.* **294**, 81. DOI. ADS.

Vibert, D., Peillon, C., Lamy, P., Frazin, R.A., Wojak, J.: 2016, Time-dependent tomographic reconstruction of the solar corona. *Astron. Comp.* **17**, 144. DOI. ADS.